



Biomimetic manganese-based theranostic nanoplatform for cancer multimodal imaging and twofold immunotherapy

Yuyue Zhao^{a,1}, Yuanwei Pan^{b,c,1}, Kelong Zou^{a,1}, Zhou Lan^{a,1}, Guowang Cheng^d, Qiuying Mai^d, Hao Cui^a, Qianfang Meng^b, Tongkai Chen^d, Lang Rao^b, Limin Ma^{e,**}, Guangtao Yu^{a,*}

^a Stomatological Hospital, Southern Medical University, Guangzhou, 510280, China

^b Institute of Biomedical Health Technology and Engineering, Shenzhen Bay Laboratory, Shenzhen, 518132, China

^c Departments of Diagnostic Radiology, Surgery, Chemical and Biomolecular Engineering, and Biomedical Engineering, Yong Loo Lin School of Medicine and Faculty of Engineering, National University of Singapore, Singapore, 119074, Singapore

^d Science and Technology Innovation Center, Guangzhou University of Chinese Medicine, Guangzhou, 510405, China

^e Medical Research Center, Guangdong Provincial People's Hospital, Guangdong Academy of Medical Sciences, Guangzhou, 510080, China

ARTICLE INFO

Keywords:

Biomimetic
Manganese ions
The second near-infrared window
Cancer imaging
Immunotherapy

ABSTRACT

The limited clinical response and serious side effect have been challenging in cancer immunotherapy resulting from immunosuppressive tumor microenvironment (TME) and inferior drug targeting. Herein, an active targeting TME nanoplatform capable of revising the immunosuppressive TME microenvironment is designed. Briefly, gold nanorods (GNRs) are covered with silica dioxide (SiO₂) and then coated manganese dioxide (MnO₂) to obtain GNRs@SiO₂@MnO₂ (GSM). Myeloid-derived suppressor cells (MDSCs) membrane is further camouflaged on the surface of GSM to obtain GNRs@SiO₂@MnO₂@MDSCs (GSMM). In this system, GSMM inherits active targeting TME capacity of MDSCs. The localized surface plasmon resonance of GNRs is developed in near-infrared II window by MnO₂ layer coating, realizing NIR-II window photothermal imaging and photoacoustic imaging of GSMM. Based on the release of Mn²⁺ in acidic TME, GSMM can be also used for magnetic resonance imaging. In cancer cells, Mn²⁺ catalyzes H₂O₂ into ·OH for (chemodynamic therapy) CDT leading to activate cGAS-STING, but also directly acts on STING inducing secretion of type I interferons, pro-inflammatory cytokines and chemokines. Additionally, photothermal therapy and CDT-mediated immunogenic cell death of tumor cells can further enhance anti-tumor immunity via exposure of CRT, HMGB1 and ATP. In summary, our nanoplatform realizes multimodal cancer imaging and dual immunotherapy.

1. Introduction

Immunotherapy, especially immune checkpoint blockade (ICB) therapy, has revolutionized progress in cancer treatment [1]. However, low potency ratio and response ratio account for failure of immunotherapy attributing to poor tumor targeting and cold tumor, characterized shortage of pro-inflammatory immune cells, inadequate exposure to tumor antigens and immunosuppressive tumor microenvironment (TME) [2]. Noteworthy, combing nanotechnology with immunotherapy is becoming star treatment to convert cold tumor into hot tumor

[3].

Photothermal therapy (PTT), utilizing photothermal agents to convert photonic into thermal energy and trigger local heat effect, has rapidly developed for cancer treatment in the past decades [4]. The photothermal agents in the second near-infrared (NIR-II, 1000–1700 nm) window bring more attention due to its deeper tissue penetration and higher imaging resolution in recent years [5]. Therefore, the research and development of photothermal agents in the NIR-II window has become a hotspot. Recently, gold-based nanomaterials have attracted much attention due to photoacoustic imaging (PAI) and PTT abilities

Peer review under responsibility of KeAi Communications Co., Ltd.

* Corresponding author.

** Corresponding author.

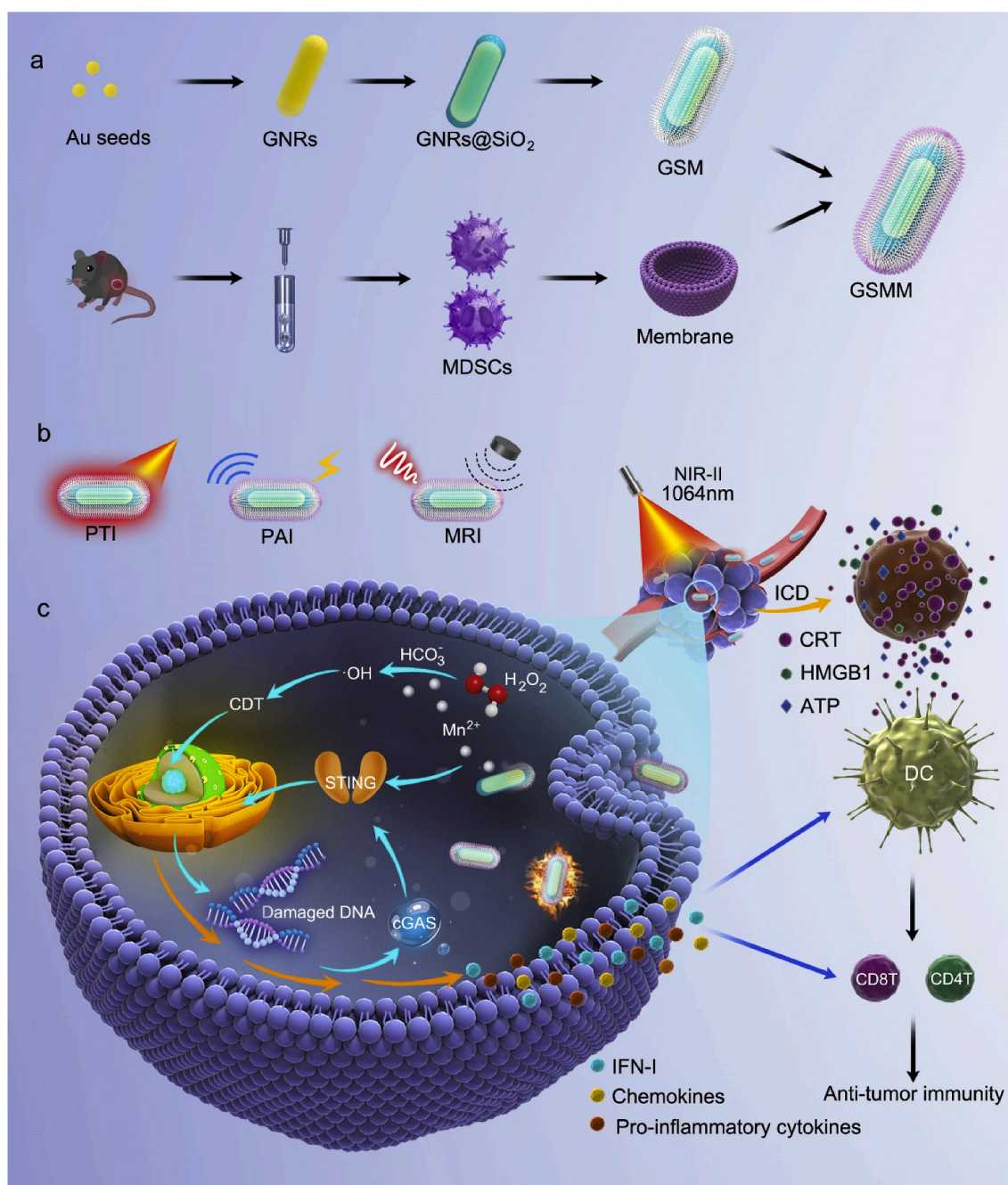
E-mail addresses: malimin7@126.com (L. Ma), guangtao1986@smu.edu.cn (G. Yu).

¹ These authors contributed equally to this work.

<https://doi.org/10.1016/j.bioactmat.2022.04.011>

Received 16 February 2022; Received in revised form 1 April 2022; Accepted 12 April 2022

2452-199X/© 2022 The Authors. Publishing services by Elsevier B.V. on behalf of KeAi Communications Co. Ltd. This is an open access article under the CC BY-NC-ND license (<http://creativecommons.org/licenses/by-nc-nd/4.0/>).



Scheme 1. The multimodal imaging and dual immunotherapy of GSMM. (a) Schematic diagram of the fabrication of GSMM nanoplateform. (b) The applications for PTI, PAI and MRI of GSMM. (c) The mechanism of GSMM for enhancing anti-tumor immunity via Mn²⁺ directly or indirectly (catalyzes H₂O₂ into ·OH leading to CDT) activates STING signaling pathway and PTT inducing ICD. (GSMM: GNRs@SiO₂@MnO₂@MDSCs; PTI: Photothermal imaging; PAI: Photoacoustic imaging; MRI: Magnetic resonance imaging; CDT: Chemo-dynamic therapy; PTT: photothermal therapy; ICD: Immunologic cell death).

owing to its unique plasmonic, acoustic, electric and morphological properties [6]. Presently, some research demonstrated the tunable localized surface plasmon resonance (LSPR) ability in NIR-II region of gold nanomaterials, which endowed its numerous applications in tumor theranostics [6,7]. Given a single strategy cannot completely eliminate the tumor, combinatorial strategies are being developed. Chemo-dynamic therapy (CDT) is a new kind of tumor treatment technology based on Fenton like reaction, which is widely used in the development of anti-tumor nano-drugs [8]. Manganese, an essential metal element for human body, is one of the most commonly used materials in design and synthesis of multifunctional cancer theranostics agent [9,10]. For instance, manganese dioxide (MnO₂) is commonly

used as a catalase to eliminate hydrogen peroxide (H₂O₂) and produce ROS to kill cancer cells via the released manganese ions (Mn²⁺) inducing Fenton-like reaction in TME [11]. Mechanism research revealed that PTT and CDT could improve anti-tumor immunity via inducing immunogenic cell death (ICD) of tumor cells accompanied by the expression Calreticulin (CRT) and the release of high-mobility group box 1 (HMGB1) as well as ATP [12]. In addition to being a CDT agent, Mn²⁺ is also one of the best alternative agents for T₁-weight magnetic resonance imaging (MRI) of cancer [13]. Therefore, the multifunctional MnO₂ cooperated with gold nanomaterials is going to be a much more powerful cancer theranostics agent.

Emerging research has shown that the stimulator of interferon genes

(STING) signaling pathway plays a crucial role in the activation of anti-tumor immune response and remodeling TME, which switches cold tumor into hot tumor [14]. In brief, cyclic GMP-AMP synthase (cGAS) encounters damage-associated double-stranded DNA in the cytosol and catalyzes the generation of cyclic [G(2',5')pA(3',5')p] (cGAMP), which act as the second messenger to activate STING and then produce type I interferons [IFN-I: interferons α (IFN α) and interferons β (IFN β)], pro-inflammatory cytokines and chemokines, such as interleukin 6 (IL-6), tumor necrosis factor α (TNF- α), Chemokine (C-X-C motif) Ligand 10 (CXCL10) [15,16]. Recent evidence has demonstrated that the metal ions play a vital role in regulation of immunity, such as Ca^+ inhibits adenosine metabolism, Zn^{2+} enhances the anti-tumor effect T cells, Mn^{2+} activates cGAS-STING signaling pathway [17–20]. More importantly, some treatment strategies based on Mn^{2+} have made significantly progress in clinical trials, such as a completed phase 1 clinical trial (ClinicalTrials.gov, NCT03991559) shows Mn^{2+} enhances anti-immune response in multidrug-resistant patients with advanced metastatic solid tumor via promoting IFN-I, IL-6, IL-8, TNF- α secretion [21]. Additionally, Mn^{2+} was also proved to be able to synergize chemotherapy, ICB and *in situ* vaccine [22–24].

Based on the peculiarity of gold, manganese nanomaterials and our previous biomimetic engineering experiences [25,26], we firstly constructed composite nanoparticles of MnO_2 coating gold nanorod (GNR) with the help of silicon dioxide (SiO_2). Then, the composite nanoparticles GNR@ SiO_2 @ MnO_2 (hereafter referred to as GSM) was coated myeloid-derived suppressor cells (MDSCs) membrane, which can actively target TME [27], to construct the ultimate multi-functional nano-theranostics agent (GNR@ SiO_2 @ MnO_2 @MDSCs, hereafter referred to as GSMM) (Scheme 1). With the coating MnO_2 on the GNR surface, the GSMM showed the capabilities of NIR-II window photonic hyperthermia. Besides, the GSMM inherited the PAI and MRI abilities based on the degradation of MnO_2 layer for cancer imaging in TME. More importantly, the GSMM could enhance anti-tumor immunity depending on multiple methods to realize dual immunotherapy: (1) Mn^{2+} released from GSMM catalyzed H_2O_2 into hydroxyl radical ($\cdot\text{OH}$, a kind of ROS) for CDT leading to activate c-GAS-STING signaling, Mn^{2+} directly acts on STING inducing secretion of IFN-I, pro-inflammatory cytokines and chemokines; (2) PTT and CDT-mediated ICD to enhance anti-tumor immune response via CRT, HMGB1 and ATP, which promotes the maturity of dendritic cell (DC) and antigen presentation.

2. Materials and methods

2.1. Reagents

Chloroauric acid ($\text{HAuCl}_4 \cdot 3\text{H}_2\text{O}$) and tetraethyl orthosilicate (TEOS) were purchased from Sigma-Aldrich. Ascorbic acid (AA) and silver nitrate (AgNO_3) were purchased from Sinopharm Chemical Reagent Ltd. (Shanghai, China). Cetyltrimethyl ammonium bromide (CTAB) and sodium borohydride (NaBH_4) were purchased from Aladdin Reagent Co. Ltd. (Shanghai, China). Potassium permanganate (KMnO_4) was purchased from Lingfeng chemical reagent CO. Ltd. (Shanghai, China).

2.2. Preparation of gold nanorods (GNRs)

The seed solution for GNRs was prepared as reported previously [6]. Briefly, a 166.7 μL amount of 5 mM HAuCl_4 , 2.5 mL of 100 mM CTAB and 466 μL ultra-pure water were mixed together. A 200 μL of fresh 10 mM NaBH_4 was quickly injected into the above solution under vigorous stirring (1200 rpm). The stirring was stopped after 2 min to obtain gold seeds solution, the solution color changed from yellow to brownish-yellow. The seed solution was aged at 37 °C for 30 min before use. The GNRs grew in a solution consisting of 50 mL of 100 mM CTAB, 5 mL of 5 mM HAuCl_4 , 500 μL of 100 mM AA, 1 mL of 500 mM H_2SO_4 , and 500 μL of 10 mM AgNO_3 . The solution was stirred at 600 rpm for 2 min, then 120 μL of seed solution was added to initiate the growth. The

reaction was kept at 37 °C overnight. The GNRs were harvested by centrifugation and washed them repeatedly with ultra-pure water to remove the excess CTAB. The GNRs were redispersed with 25 mL ultra-pure water.

2.3. Preparation of GNRs@ SiO_2 @ MnO_2 (GSM)

The mesoporous silica coating on GNRs were synthesized according to a literature procedure [6]. Briefly, 5 mL of as synthesized GNRs solution was diluted to 20 mL with ultra-pure water, then adjusted to pH = 10 by 28 wt% ammonia. Afterward, TEOS (10 w% in ethanol, 30 μL) was added into the above solution under gentle stirring. The procedure was repeated four times with 30 min intervals. Then the whole system was continually stirred for 24 h at 30 °C. The GNR@ SiO_2 was washed by centrifugation and redispersed with 10 mL of ultra-pure water. Then 8 mL of 4 mM KMnO_4 was dropwise added into the suspension of GNR@ SiO_2 under ultrasonication. After 24 h, the GNR@ SiO_2 @ MnO_2 nanoparticles were obtained by centrifugation and redispersed with ultra-pure water.

2.4. Myeloid derived suppressor cells (MDSCs) isolation

MDSCs Isolation Kit (mouse) was purchased from Miltenyi Biotec (German). Firstly, the femur was dissected from tumor-bearing C57BL/6 mouse. Then, the cells in bone marrow cavity were collected by means of irrigation and then filtered with 70- μm cell strainers (Becton & Dickinson). Next, the cell suspension was indirectly magnetically labeled with Anti-Gr-1-Biotin and anti-Biotin microBeads. Then, the cell suspension is loaded on to a MACS column, which is placed in the magnetic field of a MACS Separator. The magnetically labeled cells are retained with the column. After removing the column from the magnetic field, the magnetically labeled cells were collected in a 15 mL centrifuge tube. To increase the purity of MDSCs, repeat the magnetic separation procedures as above steps. Finally, cells were fluorescently stained with CD11b (BD, BB515, clone M1/70) and Gr-1 (BD, BV650, clone RB6-8C5) and analyzed by flow cytometry to confirm the purity of MDSCs. Cell debris and dead cells were excluded from the analysis based on scatter signals and propidium iodide fluorescence.

2.5. Preparation of GNRs@ SiO_2 @ MnO_2 @MDSCs (GSMM)

Membrane coating was prepared as our previous literature [26,28]. Briefly, MDSCs were disrupted using a Dounce homogenizer. The entire solution was subjected to 20 passes before spinning down at 3200g for 5 min. The supernatants were saved and centrifuged at 20000g for 30 min, after which the pellet was discarded and the supernatant was centrifuged again at 80000g for 2 h using an ultra-speed centrifuge (LE-80 K, Beckman Coulter, USA). The pellets containing the cell membranes were washed once in 1 mM EDTA and 10 mM Tris-HCl, and then collected as purified MDSCs membranes. Then MDSCs membrane-vesicles were obtained by physically extruding the pellets for several passes through 400 nm and 200 nm microporous membranes with an Avanti mini-extruder (Avanti Polar Lipids, USA). Subsequently, the MDSCs membrane-vesicles and GSM were mixed and extruded 11 times through a 200 nm microporous membranes and excess MDSCs membrane-vesicles were removed by centrifugation to obtain GSMM.

2.6. Characterization of GSMM

Transmission electron microscopy (TEM) images were acquired by Talos F200X. The UV–vis absorption spectra was measured on a UV–vis spectrophotometer (Agilent, Cary5000). The dynamic light scattering (DLS), and Zeta potential experiments were carried out using a Zetasizer Nano-ZS (Malvern Instruments).

2.7. Photothermal properties

To evaluate the photothermal properties, 200 μL water containing different concentration GSMM and GSM solution (0, 10, 20, 40, 80, 100 ppm based on Au) were irradiated under a 1064 nm laser (BEIJING LASERWAVE OPTOELECTRONICS TECHNOLOGY) with power density of 0.6 W/cm^2 . Then, the 200 μL water containing 80 ppm GSMM and GSM solution was irradiated under a 1064 nm laser with different power density (0.2, 0.4, 0.6, 0.8, 1.0 W/cm^2). The real-time temperature was recorded using infrared thermal imager (Fotric, Beijing, China). The photothermal stability of GSMM and GSM were tested by six cycles of laser irradiation “on” and “off” (80 ppm, 0.6 W/cm^2).

2.8. SDS-PAGE

For sodium dodecyl sulfate-polyacrylamide gel electrophoresis (SDS-PAGE), GSM, MDSCs membrane, and GSMM were added into the protein extraction buffer and the protein contents were measured with a bicinchoninic acid (BCA) kit (Sigma-Aldrich). The samples were heated at 95°C for 5 min and 20 μg of each sample was loaded into a 10% SDS-polyacrylamide gel. The samples were run at 120 V for 1.5 h and the gel was stained with Coomassie blue for 4 h and then decolorated overnight before taking pictures.

2.9. Cell lines

B16/F10, RAW 264.7, 4T1 and HOK were purchased from the American Type Culture Collection (ATCC, Manassas, VA) and genotype confirmed using STR sequence. Cell lines were maintained in Dulbecco's modified Eagle's medium (DMEM), 10% fetal bovine serum (FBS), at 5% CO_2 and 37°C in a humidified incubator according to ATCC guidelines.

2.10. Animal

All experimental procedures were approved and performed in accordance with the guidelines of Institutional Animal Care and Use Committee of Southern Medical University. All mice were purchased from the Experimental Animal Center of Southern Medical University. All mice were fed in the Specified Pathogen Free (SPF) environment.

2.11. RNA sequencing

B16/F10 were inoculated into 6-well plates at a density of 5×10^6 cells/well and cultured overnight. Then, these cells were incubated with or without GSMM (80 ppm) for 4 h. Subsequently, total RNA was extracted from cells using Trizol (Life Technologies, CA, USA). RNA integrity was assessed using the RNA Nano 6000 Assay Kit of the Bioanalyzer 2100 system (Agilent Technologies, CA, USA). A total amount of 1 μg RNA per sample was used as input material for the RNA sample preparations. Sequencing libraries were generated using NEBNext® Ultra™ RNA Library Prep Kit for Illumina® (NEB, USA) following manufacturer's recommendations and index codes were added to attribute sequences to each sample. The clustering of the index-coded samples was performed on a cBot Cluster Generation System using TruSeq PE Cluster Kit v3-cBot-HS (Illumina) according to the manufacturer's instructions. After cluster generation, the library preparations were sequenced on an Illumina Novaseq platform and 150 bp paired-end reads were generated. Feature Counts v1.5.0-p3 was used to count the reads numbers mapped to each gene. And then FPKM of each gene was calculated based on the length of the gene and reads count mapped to this gene. FPKM, expected number of Fragments Per Kilobase of transcript sequence per Millions base pairs sequenced, considers the effect of sequencing depth and gene length for the reads count at the same time, and is currently the most commonly used method for estimating gene expression levels. Gene Ontology (GO) enrichment analysis of differentially expressed genes was implemented by the cluster Profiler R

package, in which gene length bias was corrected. GO terms with corrected P value less than 0.05 were considered significantly enriched by differential expressed genes. KEGG is a database resource for understanding high-level functions and utilities of the biological system from molecular-level information. Cluster Profiler R package was used to test the statistical enrichment of differential expression genes in KEGG pathways.

2.12. RT-PCR

B16/F10 were inoculated into 6-well plates at a density of 5×10^6 cells/well and cultured overnight. Then, these cells were incubated with or without GSMM (80 ppm) for 4 h. Subsequently, total RNA was extracted from cells using Trizol (Life Technologies, CA, USA). Quantitative real-time PCR was performed in triplicate with an Applied LightCycler 96 quantitative PCR system (Roche). The primer and probe sequences were as follows: Inf β 1 forward primer, 5'-CTGGCTTCCAT-CATGAACAA-3', Inf β 1 reverse primer, 5'-AGAGGGCTGTGGTGGAGAA-3'; Gapdh forward primer, 5'-GAAGGTGAAGGTCGGAGTCA-3', Gapdh reverse primer, 5'-TTGAGGTCAATGAAGGGTC-3'.

2.13. Western blotting

Western blot was performed as previously described [29]. Briefly, the samples were lysed $1 \times$ SDS-PAGE loading buffer and then the lysates were resolved by SDS-PAGE and transferred to polyvinylidene difluoride (PVDF) membranes. Afterward, the PVDF membranes were incubated with STING, p-SING, p-TBK1 and p-IRF3 (CST). The chemiluminescence detection reagents (Merck Millipore, Billerica, MA) were used for imaging.

2.14. Methylene blue (MB) assay

To evaluate the generation of $\cdot\text{OH}$ by GSMM, 80 $\mu\text{g/mL}$ of GSMM, 10 $\mu\text{g/mL}$ MB, 25 mM NaHCO_3 and 10 mM H_2O_2 was mixed by different permutation and combination (G1: MB, G2: MB + H_2O_2 , G3: MB + GSMM, G4: MB + GSMM + H_2O_2 , G5: MB + GSMM + H_2O_2 + NaHCO_3). After 30 min incubation, the solution absorbance was measured at 663 nm.

2.15. CCK-8 assay

B16/F10 cells were seeded in 96-well plates at a density of 5×10^3 cells per well and incubated for 24 h. And then, the cells were washed by PBS and incubated with different concentration of GSMM (0, 5, 10, 20, 40 and 80 $\mu\text{g/mL}$). Five replicate wells were designed for each concentration. After 4 h incubation, one-third of wells were irradiated with a 1064 nm laser (0.6 W/cm^2) for 5 min and another one-third of wells were treated for 10 min. Subsequently, the cells were continuously incubated for 20 h and then the cell viabilities were measured by CCK8 according to manufacturer's instructions.

2.16. ROS assay

DCFH-DA fluorescence probe was used to measure the ROS generation. B16/F10 cells were inoculated into 6-well plates at a density of 1×10^6 cells/well and cultured overnight. The next day, B16/F10 cells were treated with different concentrations of GSMM (0, 5, 10, 20 and 40 $\mu\text{g/mL}$) for 2 h. And then, DCFH-DA fluorescence probe (10 μM) was added to the medium for 30 min. Afterward, the cells were washed twice with PBS and observed by laser scanning confocal microscope (Leica SP8).

2.17. In vitro PTT assay

B16/F10 cells were inoculated into 6-well plates at a density of 1×10^6 cells/well and cultured 24 h. The next day, the cells were incubated

with different treatments (Group 1: PBS; Group 2: PBS; Group 3: GSM, 40 $\mu\text{g}/\text{mL}$; Group 4: GSMM, 40 $\mu\text{g}/\text{mL}$; Group 5: GSMM, 40 $\mu\text{g}/\text{mL}$). After 4 h incubation, Group 2, 3 and 5 were irradiated with a 1064 nm laser ($0.6 \text{ W}/\text{cm}^2$) for 10 min. Subsequently, the cells were continuously incubated for 20 h and then the cell live or dead were measured by Calcein-AM/PI kit according to manufacturer's instructions (BestBio, Shanghai, China). Additionally, the cell climbing slices were prepared with the same treatment as above and then fixed for the expression of CRT by immunofluorescence in each group. The cell supernatant was

collected and the level of ATP and HMGB1 were measured by enzyme-linked immunosorbent assay (ELISA) kit according to manufacturer's instructions (Absin, Shanghai, China).

2.18. In vivo pharmacokinetics and biodistribution

To study the pharmacokinetics of nanoparticles, C57BL/6 mice ($n = 4$ each group) received an intravenous (i.v.) injection of 200 μL PBS containing GSMM or GSM at a dose of 5 mg/kg based on Au. At various

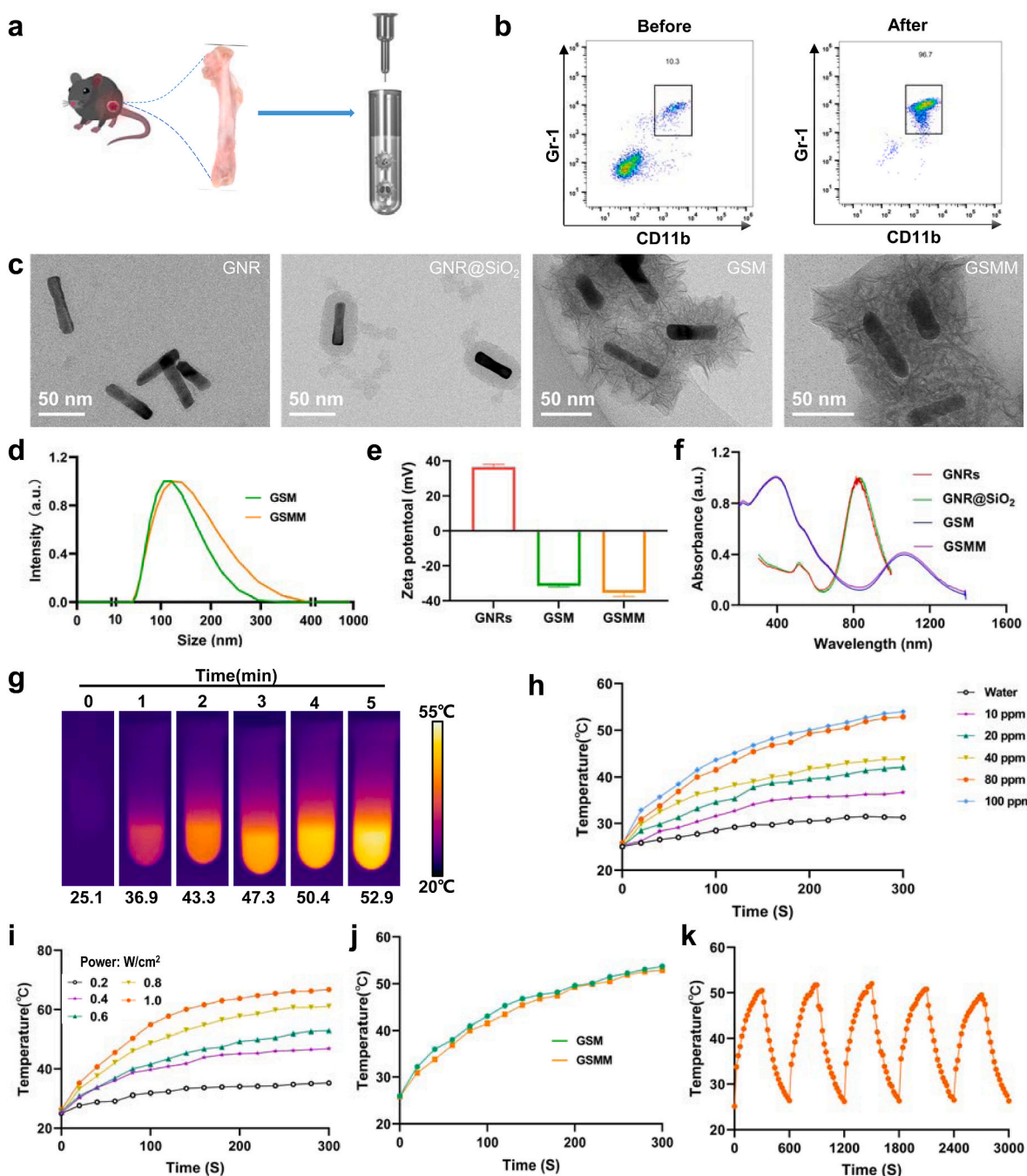


Fig. 1. Characterization of GSMM. (a) Schematic illustration of the sorting route for MDSCs. (b) Flow images of MDSCs at before or after magnetic cell sorting. (c) TEM images of GNR, GNR@SiO₂, GSM and GSMM. (d) Hydrodynamic size distribution of GSM and GSMM measured by dynamic light scattering. (e) Zeta potential of GNR, GSM and GSMM. (f) UV-vis-NIR spectra of GNR, GNR@SiO₂, GSM and GSMM. (g) Photothermal images of GSMM in different time points under a 1064 nm laser irradiation (80 $\mu\text{g}/\text{mL}$, $0.6 \text{ W}/\text{cm}^2$). (h) The heating curve of GSMM with different concentration (0, 10, 20, 40, 80, 100 ppm) under a 1064 nm laser irradiation (0.6 W/cm^2). (i) The heating curve of GSMM with different laser powers (0.2, 0.4, 0.6, 0.8, 1.0 W/cm^2) under a 1064 nm laser irradiation (80 ppm). (j) The photothermal stability of GSMM after six cycles of laser irradiation “on” and “off”. (k) The heating curve of GSM and GSMM under a 1064 nm laser irradiation (80 ppm, $0.6 \text{ W}/\text{cm}^2$).

time points after the injection, 50 μL blood was collected via the tail veins, and then Au content was quantified with ICP-MS. For bio-distribution, tumor-bearing C57BL/6 mice ($n = 3$ each group) received an intravenous (i.v.) injection of 100 μL PBS containing GSMM or GSM at a dose of 5 mg/kg based on Au. All mice were euthanized on the 24 h after the injection and their hearts, livers, spleens, kidneys, lungs, and tumor were dissociated. Organs were weighed and then Au content of organs was quantified with ICP-MS.

2.19. In vivo biosafety

In order to test the biosafety of GSMM, C57BL/6 mice ($n = 5$ each group) received an i.v. injection of 100 μL PBS, or PBS containing GSMM at a dose of 5 mg/kg based on Au. General status of the mice was evaluated every day by veterinarians and mice body weights were measured every other day. All mice were euthanized on the 14th day after the injection and their blood samples and major organs, including hearts, livers, spleens, lungs and kidneys, were collected. Three important hepatic indicators and two primary indicators for kidney functions were measured by using a blood biochemical autoanalyzer (7080, HITACHI, Japan). The complete blood panel data from healthy control and treated mice were also tested. Organs were fixed in 4% neutral buffered formalin, processed routinely into paraffin and sectioned at 6 μm . Then the sections were stained with hematoxylin and eosin (H&E), and scanned using Aperio VERSA (Leica, Germany).

2.20. In vivo imaging

To establish tumor-bearing C57BL/6 mouse model, B16/F10 cells (2.5×10^5 cells in 100 μL serum-free cell medium) were injected subcutaneously into the flank of C57BL/6 mouse. BALB/c nude mice xenografts were obtained by subcutaneous (s.c.) injection of 50 μL serum-free cell medium containing 1×10^5 B16/F10 cells into the shoulder of mice. After the tumor volume reached 100 mm^3 , the tumor-bearing mice were used for further experiments. Tumor volumes were calculated according to the following equation: (tumor length) \times (tumor width)²/2.

For magnetic resonance imaging (MRI), tumor-bearing C57BL/6 mouse received an intravenous (i.v.) injection of 200 μL PBS or PBS containing GSMM or GSM at a dose of 5 mg/kg based on Au. The T1-weighted MRI was acquired at various time points (0, 1, 4 and 24 h) via a high magnetic field micro-MR scanner (PharmaScan 7.0 T, Bruker, Germany).

For photoacoustic imaging (PAI), tumor-bearing BALB/c nude mice were injected with 200 μL PBS containing GSMM or GSM at a dose of 5 mg/kg based on Au. The photoacoustic signal in mice were acquired at different time points (0, 1, 4, 8, 12 and 24 h) by a photoacoustic imaging system (LOIS-3D, TomoWave Laboratories, USA) with 1064 nm laser (180mJ/pulse).

For *in vivo* fluorescence imaging, firstly, DIR marked RBC (RBC^{DIR}), MDSCs membrane (MDSCs^{DIR}) and GSMM (GSMM^{DIR}) were prepared according to manufacturer's instructions. And then tumor-bearing C57BL/6 mouse received an intravenous (i.v.) injection of 100 μL PBS containing RBC^{DIR}, MDSCs^{DIR} and GSMM^{DIR}. The fluorescence signal in mice were acquired at different time points (1, 2, 4, 6 and 24 h) by *In-Vivo* FX PRO (Bruker, Germany).

2.21. In vivo treatment

Tumor-bearing C57BL/6 mouse were randomly separated into five groups ($n = 5$ per group), including G1: PBS, G2: PBS + Laser, G3: GSM + Laser, G4: GSMM, G5: GSMM + Laser. After 4 h injected with GSMM (5 mg/kg based on Au), GSM (5 mg/kg based on Au) or PBS, the mice were treated with a 1064 nm laser (0.6 W/cm²) for 10 min in G2, 3 and 5. The real-time temperature in tumor was recorded using infrared thermal imager (Fotric, Beijing, China). All mice were treated every five days. The body weights and tumor volume of mice were monitored

every two days for ten days. Whereafter, the mice injected euthanasia and the tumors were dissected. Partial tumor specimens were fixed in 4% neutral buffered formalin, processed routinely into paraffin and sectioned at 4 μm . Then, the tumor sections were stained with Ki67 and Calreticulin (CST). Partial tumor tissues were used for following western blotting and flow cytometry.

2.22. Flow cytometry

For flow cytometric analysis, single cell suspensions were first prepared. The tumor tissues were dissected from mice. And then, the tumor was placed in C Tube containing the enzyme mix (DNases: 25 U/mL, Sigma-Aldrich; collagenase IV: 0.2 mg/mL, Sigma-Aldrich and hyaluronidase: 0.1 mg/mL, Sigma-Aldrich) to cut into small pieces using gentleMACS™ Tissue Dissociators, and go on digesting in incubator at 37 °C for 1 h, and were then filtered with 70- μm cell strainers (Becton & Dickinson). Subsequently, the cells were stained with following antibodies: Live/Dead (AF700), CD45 (APC-Cy7; clone 30-F11), CD3 (BV510, clone 145-2c11), CD8a (BB515; clone 53-6.7), CD4 (BB700; clone RM4-5), CD11b (APC; clone M1/70), Gr-1 (BV650; clone RB6-8C5), F4/80 (BV421; clone BM8), CD206 (BV785; clone BM8), CD11c (PE-CY7; clone B-ly6) and CD86 (PE; clone GL1) (all from Becton & Dickinson). The samples were measured using a CytoFLEX flow cytometer (Beckman). The results were analyzed using FlowJo (Tree Star).

2.23. Statistical analysis

Data analyses were performed using Graph Pad Prism version 9.0 for Windows (Graph Pad Software Inc, La Jolla, CA). Unpaired *t*-test, one-way ANOVA with Dunnett's multiple comparison tests and two-way ANOVA with Tukey's or Sidak's multiple comparisons test was used to analyze significant differences. Dates were represented as the mean \pm SEM. Differences ($p < 0.05$) were considered statistically significant.

3. Results and discussion

3.1. Preparation and characterization of GSMM

The preparation of GSMM briefly includes four main steps according to the previous research [6,26]: (1) GNRs were prepared by gold seed solution approach by CTAB, HAuCl₄, AA, H₂SO₄ and AgNO₃. (2) coating a layer of SiO₂ on the surface of GNRs to obtain GNR@SiO₂ by tetraethoxysilane (TEOS) hydrolysis reaction. (3) the KMnO₄ was dropwise added into the suspension of GNR@SiO₂ under ultrasonication to acquire GSM. (4) MDSCs were first sorted from bone of tumor-bearing mouse (Fig. 1a). The purity of MDSCs was quantified to be higher than 95% with flow cytometry (Fig. 1b). Afterward, the membrane of MDSCs was prepared by hypotonic lysing and differential centrifugation, and then fused on to the outer layer of GSM to obtain GSMM.

To make sure the GSMM was successfully fabricated, the morphologies of nanoparticles were characterized by TEM and the element mapping. As shown in Fig. 1c, the dimension of GNRs was about 14 nm \times 52 nm, and the thickness of uniform SiO₂ layer around GNRs was nearly 23 nm. An irregular MnO₂ layer was clearly observed after the prepared GNRs@SiO₂ were cladded with MnO₂. The TEM images showed that the GSM nanoparticles were surrounded by a layer of membrane after coated with MDSC membranes. The element mapping displayed that Au core is surrounded with Si, Mn, and O elements in GSM (Fig. S1). Sodium dodecyl sulfate-polyacrylamide gel electrophoresis (SDS-PAGE) stripes revealed that MDSC membrane transfer did not influence the membrane protein expression in the GSMM (Fig. S2). The hydrodynamic diameter of different nanocomposites was measured by DLS (Fig. 1d), the GSM nanoparticles possessed a size of approximately 116 nm, which increased to around 129 nm after being coated with MDSC membranes. The GSMM remained stable over two weeks in FBS and PBS (Fig. S3). The zeta potentials of GNRs, GSM and GSMM are

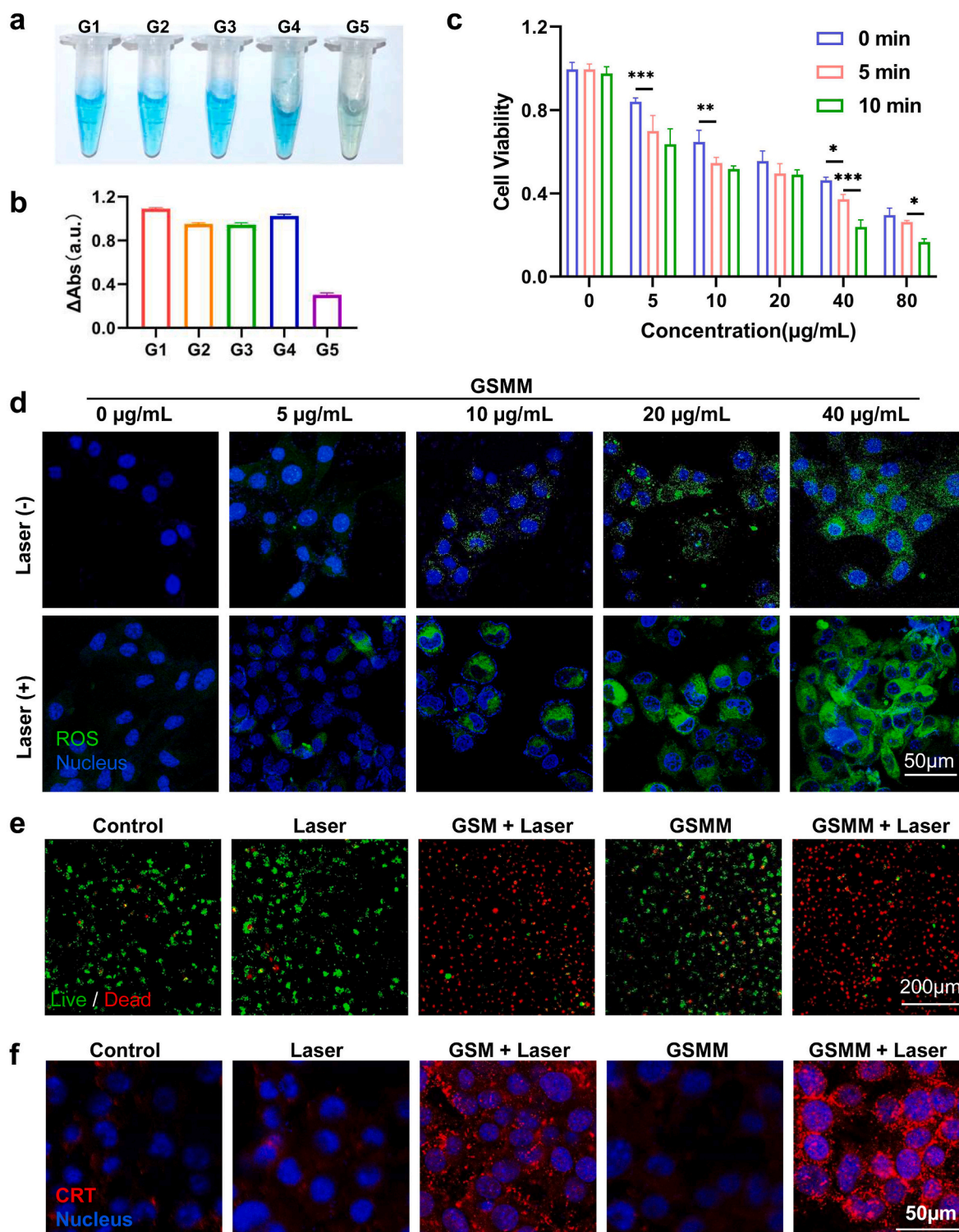


Fig. 2. The evaluation of CDT and PTT *in vitro*. (a) The images of different reaction systems. (b) The absorbance of different groups at 663 nm (G1: MB, G2: MB + H₂O₂, G3: MB + GSMM, G4: MB + GSMM + H₂O₂, G5: MB + GSMM + H₂O₂ + NaHCO₃). (c) The cell viability with different concentration GSMM co-incubation (0, 5, 10, 20, 40, 80 μ g/mL) after laser irradiation (1064 nm, 0.6 W/cm²) in different treatment time (Two-way ANOVA with Tukey's multiple comparisons test; ns: no significance, *: $p < 0.05$, **: $p < 0.01$, ***: $p < 0.001$). (d) Immunofluorescence images of ROS staining (DCFH-DA probe) of B16/F10 cells after different concentration GSMM co-incubation (0, 5, 10, 20, 40 μ g/ml) treatments with or without laser irradiation (Scale bar: 50 μ m). (e) Immunofluorescence images of live/dead staining (Calcein acetoxyethyl ester and propidium iodide probes) of B16/F10 cells with or without nanoparticles (GSM or GSMM, 80 μ g/mL) co-incubation under 1064 nm laser irradiation treatment (0.6 W/cm², 5 min). Scale bar: 200 μ m. (f) Immunofluorescence images of CRT expression on B16/F10 with or without nanoparticles (GSM or GSMM, 80 μ g/ml) co-incubation under a 1064 nm laser irradiation treatment (0.6 W/cm², 5 min). Scale bar: 50 μ m.

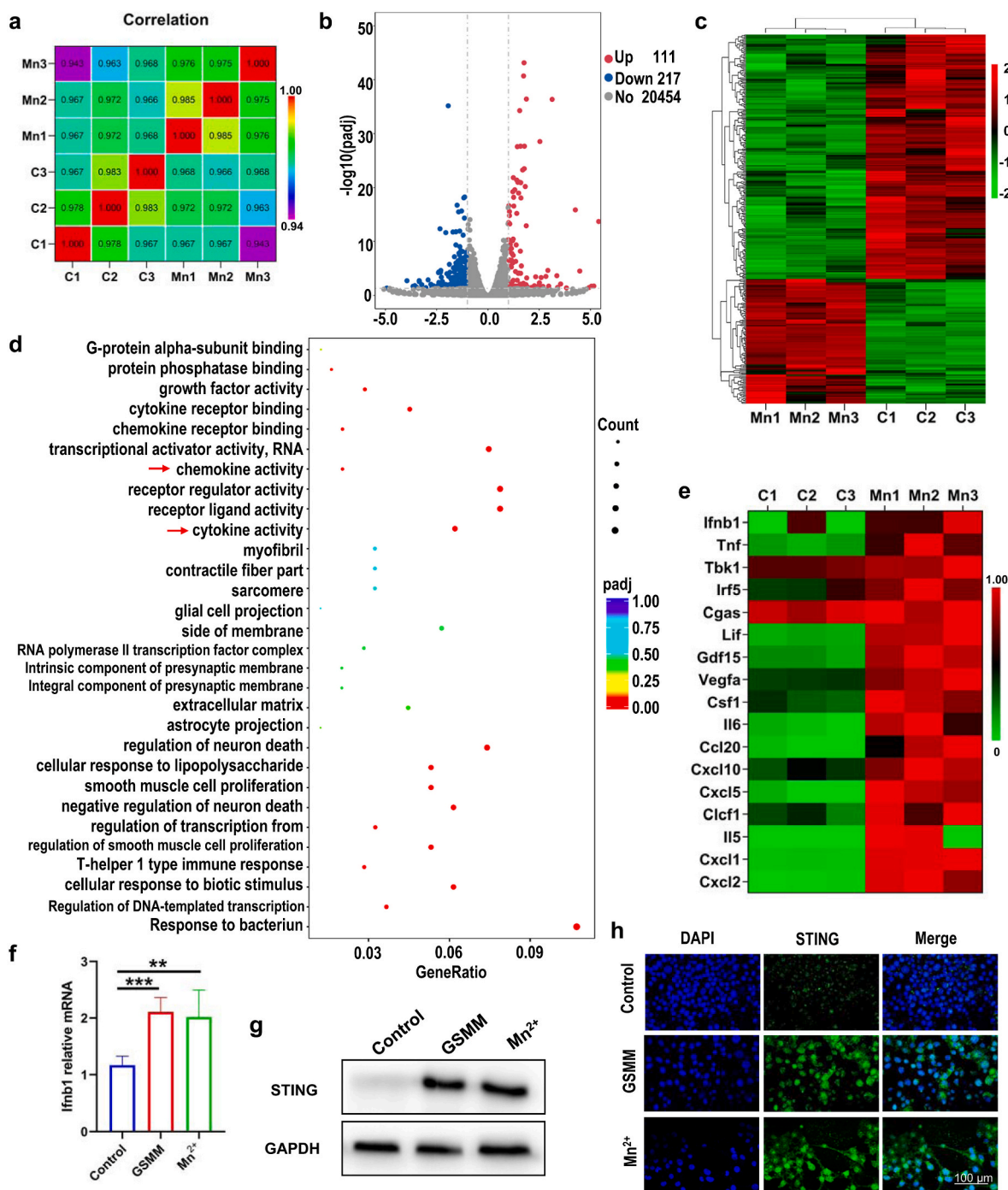


Fig. 3. The excavation of biological mechanism of GSMM by RNA sequencing. (a) Sample correlation test. (b) The volcano map of GSMM ($n = 3$: Mn1, Mn2, Mn3) and control ($n = 3$: C1, C2, C3) group. (c) The heatmap of genes alteration after GSMM treatment ($p < 0.05$, [fold change ≥ 2]). (d) Gene ontology enriched in GSMM treatment and control group (red arrows represent GSMM relative pathways). (e) The heatmap of selected genes related to cGAS-STING signaling pathway. (f) The relative mRNA expression of *ifnb1* was detected by qRT-PCR (One-way ANOVA, **: $p < 0.01$, ***: $p < 0.001$). (g) The western blotting of STING in GSMM, MnCl₂ and control group. (h) Immunofluorescence images of STING in GSMM, MnCl₂ and control group. Scale bar: 100 μm .

36.47, -31.37 , and -35.43 mV, respectively (Fig. 1e). The plasmon spectra of the nanoparticles were characterized by UV–vis–NIR spectra. As shown in Fig. 1f, the UV–vis–NIR absorption peak of GNRs exhibited at 820 nm, and negligible absorbance change after coated with SiO₂ layer. The absorption peak showed a redshift from 820 to 1066 nm with the growth of MnO₂ layer, and the characteristic absorbance of MnO₂ at 380 nm also increased. The MnO₂ layers could significantly shift the absorption peak of GSM and GSMM nanoparticles to the NIR-II region.

To explore the NIR-II region photothermal performance, the water and a series of concentration of GSMM and GSM were irradiated under a 1064 nm laser irradiation at 0.6 W/cm² for 5 min (Fig. 1g and Fig. S4a). As the concentration increased from 0 to 100 ppm, the heating curve of GSMM and GSM indicated concentration dependent peculiarity (Fig. 1h and Fig. S4b). And the peak temperature of GSMM reaches 52.7 °C, which is high enough to induce tumor cell death [30,31]. Meanwhile, the photothermal ability of GSMM and GSM also shows analogous irradiation power density dependence at a 80 ppm concentration (Fig. 1i

and Fig. S4c). More importantly, MDSC membrane transfer did not influence the photothermal ability of GSMM compared to GSM (Fig. 1j). The photothermal conversion efficiency of GSMM was calculated to be 36.4% according to the recent reported article, which exhibits excellent photothermal property (Fig. S5). The TEM imaging showed that GSMM still maintained nanorod structure after the laser irradiation (Fig. S6). Additionally, both GSMM and GSM exhibit a good photothermal stability by six-cycle laser irradiation “on” and “off” (80 ppm, 0.6 W/cm²) (Fig. 1k and Fig. S4d). And these results indicated that GSMM is an excellent NIR-II photothermal nanoplatform.

3.2. GSMM can effectively induce ICD of cancer cells

The acidic TME is an important feature of cancer [32,33]. Previous studies indicated that MnO₂ response to acidic TME leading to release of Mn²⁺ according to chemical equation: $\text{MnO}_2 + 2\text{H}^+ \rightarrow \text{Mn}^{2+} + \text{H}_2\text{O} + 1/2\text{O}_2 \uparrow$ [34]. In order to evaluate the acid sensitivity of GSMM, it was incubated in pH 6.5 buffer solution. The color of GSMM and GSM solution gradually changed from brown to light pink, which indicated Mn²⁺ was released from GSMM and GSM (Fig. S7). The TEM imaging showed that the MnO₂ shell disappears after 2 h incubation in pH 6.5 buffer solution (Fig. S8). More than 60% of Mn²⁺ is released from GSMM in pH 6.5 buffer solution at 12 h incubation, but the proportion is only 7.8% in buffer solution of pH 7.4 (Fig. S9). As is well known, Mn²⁺ could catalyzed H₂O₂ to generate ·OH with the assistance of HCO₃⁻ by Fenton-like reaction in acidic TME [35,36]. Based on Methylene blue (MB) can be degraded by ·OH, it is usually used as a dye for evaluating the level of the ·OH. Herein, the color of MB had basically disappeared in group of GSMM + H₂O₂ + NaHCO₃ (G5), but the color in other group remained blue (Fig. 2a). Meanwhile, we measured the absorbance of different groups at 663 nm (Fig. 2b). MDSCs membrane coating did not influence the acid sensitivity of GSMM compared to GSM (Fig. S10). Next, we evaluated the therapeutic effect of GSMM on B16/F10 cells. In confocal imagings, we clearly observed that GSMM or GSM could be successfully phagocytized by B16/F10 (Fig. S11). Further, the result of CCK-8 showed that the inhibition effect of cancer cell viability is concentration dependent and irradiation time dependent (Fig. 2c). And the cell viability significantly dropped to more than 60% with 40 µg/mL GSMM after laser irradiation (1064 nm, 0.6 W/cm²) in 5 min. Moreover, GSMM barely has cytotoxicity for normal cells (Fig. S12). Besides, the damaged DNA accumulated in the cells after GSMM treatment using PicoGreen dye (Fig. S13). As described above, the Mn²⁺ released from GSMM could augment the ROS level of cancer cells. Therefore, the probe 2',7'-dichlorofluorescein diacetate (DCFH-DA) was used to detect the ROS level after being incubation with different concentration GSMM for 2 h with or without laser treatment. As shown in Fig. 2d, the level of ROS indicated concentration dependent and GSMM at above 20 µg/mL concentration showed remarkably increase of ROS in B16/F10 cells. Moreover, after treated with laser irradiation, the brighter green fluorescence was detected compared to without laser treatment group, revealing the significant increases in intracellular ROS levels. Besides, based on the photothermal characteristic of GNRs, we next executed PTT for B16/F10 after 4 h incubation with GSMM or GSM. Immunofluorescence images of live/dead staining (Calcein acetoxyethyl ester and propidium iodide probes) suggested that there were almost no living cells in GSMM and GSM group after an 1064 nm laser (0.6 W/cm²) irradiation treatment for 5 min (Fig. 2e). These results show that GSMM is an excellent CDT and PTT nanoplatform *in vitro*.

Cumulative research shows that ICD has emerged as a bridge in tumor cell-microenvironment interactions by enhancing tumor cell immunogenicity [37]. The occurrence of ICD will stimulate damage-associated molecular patterns lead to release of ATP, HMGB1 and CRT for promoting anti-tumor immunity [12,38]. The experimental and clinical evidence has confirmed that certain chemotherapy, radiotherapy and PTT can act as an inducer of ICD [12]. To testify whether GSMM can induce the ICD occurrence, we measured the release of ATP,

HMGB1 and CRT in different treatment groups. The confocal images demonstrated that the expression of CRT was significantly up-regulated in GSMM + laser treatment group (Fig. 2f). The level of ATP and HMGB1 were measured by enzyme-linked immuno sorbent assay (Fig. S14). Similarly, we found that both GSMM + laser and GSM + laser treatment induced the highest level of ATP and HMGB1 release. These results suggested that GSMM is a promising agent for tumor immunotherapy.

3.3. Biological mechanism of GSMM

Next, we explored the underlying biological mechanism of GSMM for cancer cells by RNA-sequencing. The B16/F10 was treated with or without 80 ppm GSMM (three samples in each group). Correlation analysis indicated high degree of uniformity among samples in each treatment group and the gene expression is similar in the two groups (Fig. 3a). Volcano plots and hierarchical cluster revealed that 328 genes are significantly different in the GSMM treatment group compared with the control group, including 111 up-regulated genes and 217 down-regulated genes (Fig. 3b and c). For further insight into the potential targeted pathways of GSMM, we performed gene ontology (GO) analyze (Fig. 3d and Fig. S15). The results showed that cytokine activity and chemokine activity (red arrow) was high enrichment.

Recent literature identified that Mn²⁺ could significantly augment IFN- β , pro-inflammatory cytokines and chemokines by launching cGAS-STING signaling [20]. Meanwhile, the results of kyoto encyclopedia of gene and genomes (KEGG) further confirmed that certain cGAS-STING related pathways were significantly up-regulated after GSMM treatment, including chemokine signaling pathway, NF-kappa B signaling pathway, IL-17 signaling pathway and TNF signaling pathway (Fig. S16). These data suggested that GSMM could activate cGAS-STING signaling pathway. NF-kappa B RelA subunit is crucial for early IFN- β expression [39,40]. In cytoplasm, STING activates the kinases TBK1 and then induces phosphorylation of IRF, which dissociates from the adaptor proteins, dimerizes, and then enters the nucleus to induce IFN- β [41]. In deed, hierarchical cluster analysis of differential genes demonstrated that *Irf1*, *Tbk1* and *Irf5* were significantly up-regulated in GSMM treatment group (Fig. 3e). The relationship between GSMM and STING signaling pathway was further confirmed through RT-PCR (Fig. 3f), western blotting (Fig. 3g and Fig. S17) and immunofluorescence staining (Fig. 3h). The results revealed that GSMM could promote IFN- β secretion by activating cGAS-STING signaling pathway. Moreover, this biological effect of GSMM depends on Mn²⁺.

3.4. Immune escape and biosafety of GSMM

Immune escape and biosafety are necessary features for an excellent tumor imaging agent. Therefore, we incubated GSMM, and GSM with RAW264.7 murine macrophage cells for 4 h to testify the uptake of nanoparticles. The results indicated that the cellular uptake of GSM was 2–6 folds more than GSMM at all concentration tested (Fig. S18a). Then, the relationship between the uptake and the incubation time was also tested. The particle uptake significantly increased in the first 8 h, and then the uptake rate gradually slowed and reached a peak at 8–12 h (Fig. S18b). Subsequently, C57BL/6 mice were used to execute pharmacokinetic and biosafety studies *in vivo*. 100 µL GSMM and GSM was injected in to each mouse at a 25 mg Au kg⁻¹ concentration through the tail vein. At different time points after the injection, 50 µL blood was collected from the tail vein for Au-content determination by Inductively Coupled Plasma Mass Spectrometry (ICP-MS). The results showed that GSMM treatment group gave the highest Au content and consistently exhibited significantly enhanced blood retention over a span of 24 h (Fig. S18c). The results indicated that MDSCs membrane coating conferred GSMM outstanding immune escape ability, which provided a guarantee for GSMM to be better enriched in the tumor site.

To evaluate the biosafety of GSMM, the mice were treated with GSMM or PBS for continuous two weeks. The changes of body weight

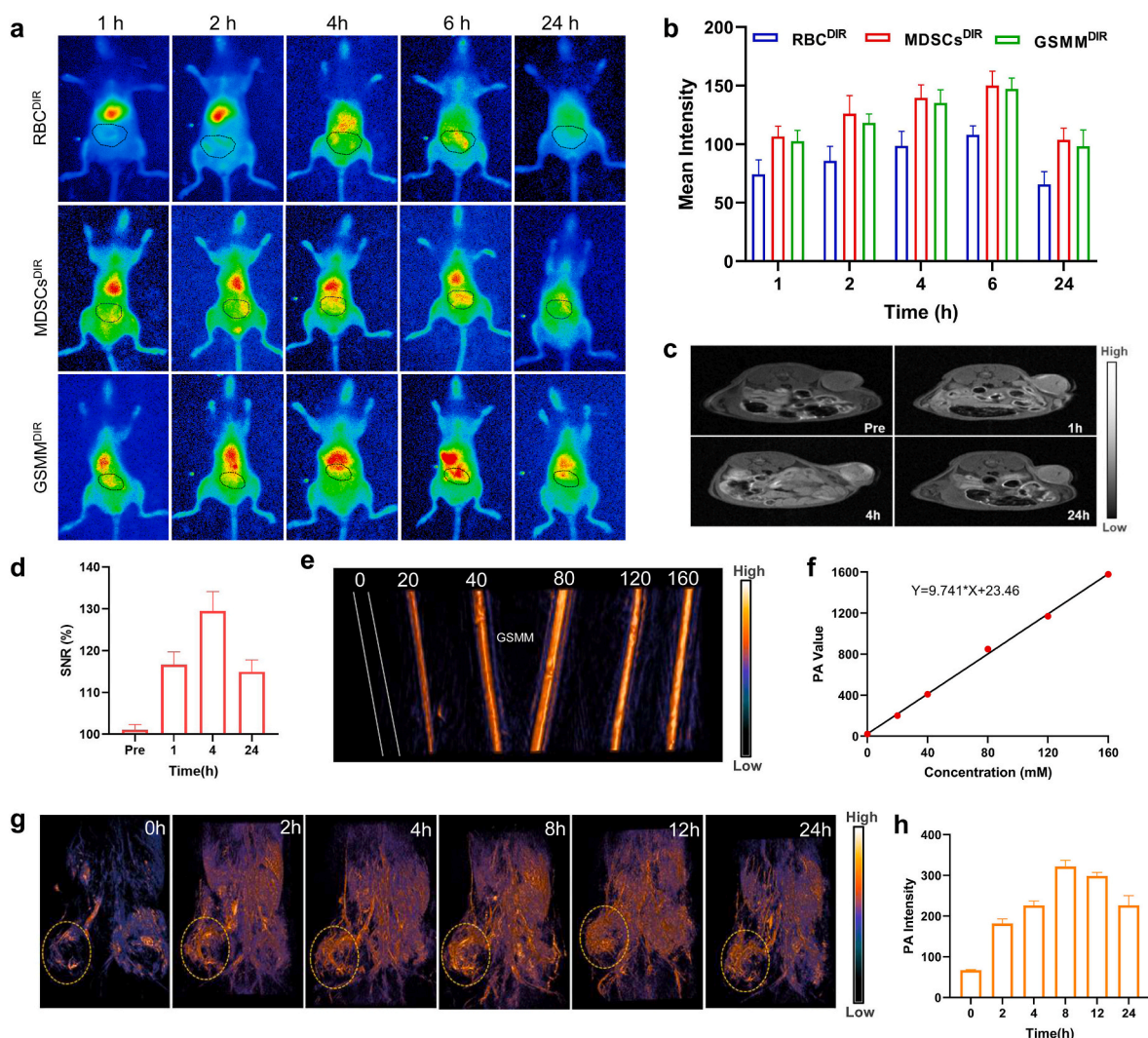


Fig. 4. The multimodal imaging of GSMM. (a) *In vivo* fluorescence images of B16F10 tumor-bearing C57BL/6 mice taken at different times post i.v. injection of RBC^{DIR} (RBC membrane marked by DIR), MDSCs^{DIR} (MDSCs membrane marked by DIR) and GSMM^{DIR} (GSMM marked by DIR). (b) Quantitative mean fluorescence intensities of tumors in different groups at various time points. (c) Representative T_1 -weight MRI images of mice injected with GSMM (i.v., 10 mg/kg) at 0, 1, 4 and 24 h. (d) The corresponding signal to noise analysis of MRI signals in tumor site at various time points. (e) The photoacoustic (PA) images of GSMM in tube with different concentrations (0, 20, 40, 80, 120 and 160 mM). (f) The simple linear regression of GSMM between concentration and PA value. (g) The PA images of B16F10 tumor-bearing nude mice injected with GSMM (i.v., 10 mg/kg) at 0, 2, 4, 8, 12 and 24 h. (h) The corresponding PA values of tumor at various time points.

were not significantly different in two groups (Fig. S19). At the end, the mice were euthanized for blood biochemistry, hematology and histological staining test. The report indicated that primary indicators of liver and kidney function, including aspartate aminotransferase (AST), alkaline phosphatase (ALP), alanine aminotransferase (ALT), creatinine (CRE) and blood urea nitrogen (BUN) barely have changed in two treatment groups, indicating that GSMM did not impact the normal function of the liver or kidney (Figs. S20a–c). Similarly, we did not discover statistically significant differences in parameters of blood routine in two treatment groups (Figs. S20d–k). Further, Hematoxylin and eosin (H&E) staining of primary organ (heart, liver, spleen, lung and kidney) also did not show any signs of abnormality in cellular morphology, inflammation, or tissue organization in the GSMM treatment group compared with control (Fig. S21). In summary, these results indicated that GSMM has excellent biosafety *in vivo*.

3.5. Multimodal imaging of GSMM

MDSCs are important members of TME which have been confirmed to be induced by tumor cells via chemokines, such as CXCL1, CXCL2

[27]. As RNA sequencing above, GSMM treatment could enhance the secretion of chemokines, including CXCL1. So, we hypothesized GSMM could actively target the TME by inheriting the ability of MDSCs. To test this hypothesis, we established a coculture system with Transwell *in vitro*. B16/F10 were seeded in the lower chamber, and GSMM or GSM were added to the upper chamber (Fig. S22a). After 12 h of incubation, the migration ratio of GSMM was significantly higher than GSM treatment group (Fig. S22b). Further, GSMM and GSM were injected into tumor-bearing C57BL/6 via tail vein and tissue uptake of the nanoparticles was measured in terms of Au content with ICP-MS. The results showed that the Au content in tumor of GSMM treatment group was significantly higher than GSM treatment group and most of nanoparticles were metabolized through liver and Spleen (Fig. S23). To further validate the tumor-targeted efficiency, GSMM, MDSCs membrane and RBC membrane labeled by DIR (denoted as GSMM^{DIR}, MDSCs^{DIR}, RBC^{DIR} respectively) were injected in to mice bearing B16/F10 xenograft for *in vivo* imaging. After 6 h injection, both GSMM^{DIR} and MDSCs^{DIR} group indicated prominent tumor enrichment compared to RBC^{DIR} group, meanwhile the fluorescence of DIR in tumor accumulation reached to pinnacle (Fig. 4a and b). *In vitro* imaging of

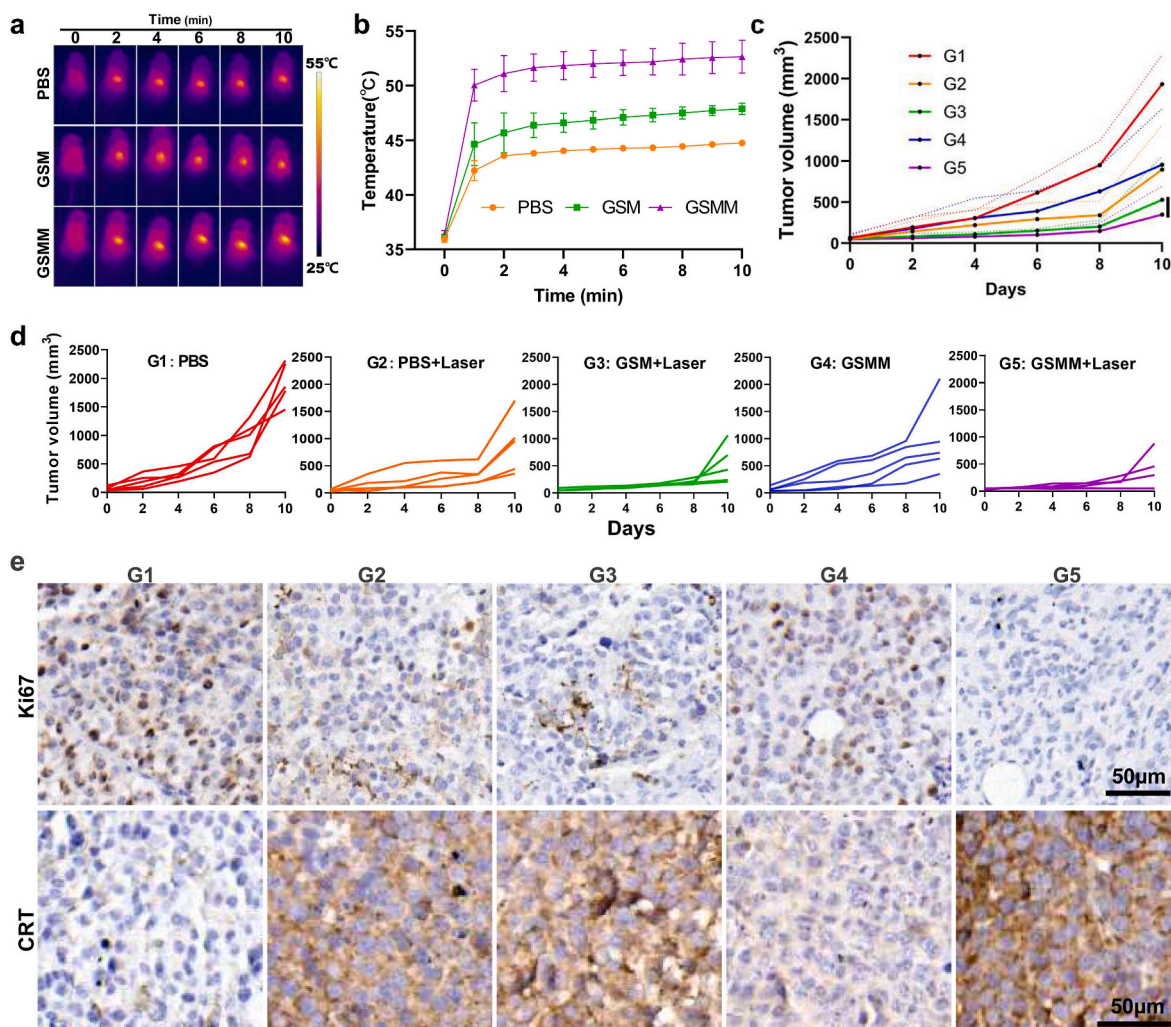


Fig. 5. *In vivo* photothermal and twofold immunotherapeutic efficacies of GSMM on B16F10 tumor-bearing C57BL/6 mice. (a) Representative thermographic images from mice under a 1064 nm laser irradiation treatment (0.6 W/cm^2) at 4 h post i.v. injection of PBS, GSM and GSMM. (b) The curve of temperature of tumor site in different groups at various time points. (c) The curve of tumor growth in different treatment groups (G1: PBS, G2: PBS + Laser, G3: GSM + Laser, G4: GSMM, G5: GSMM + Laser). (Laser irradiation was conducted at 4 h post-injection nanoparticles with a 1064 nm laser for consecutive 5 min, 0.6 W/cm^2) (Two-way ANOVA with Sidak's multiple comparisons test, G4 vs G5 at 10 days, ***: $p < 0.001$). (d) Individual tumor growth kinetics in different treatment groups. (e) The Ki-67 and CRT immunohistochemical staining images of tumor biopsies from different treatment groups. Scale bar: $50 \mu\text{m}$.

tumor and primary organs dissociated from mice after 24 h injection and quantitative analysis further showed significant tumor enrichment in GSMM^{DIR} and MDSCs^{DIR} group owing to the active targeting ability derived from MDSCs (Fig. S24). To further reveal the multimodal imaging ability of GSMM, MRI and PAI experiments were carried out. Previous studies have shown excellent enhanced MRI ability owing to release of Mn^{2+} [6,42,43]. Our imaging and signal to noise (SNR) analysis similarly indicated that MRI signal was enhanced after GSMM injection compared to before (Fig. 4c and d). And the value of SNR was higher in GSMM group than GSM group in different time points owing to MDSCs membrane coating (Fig. S25). In PAI aspect, based on the excellent photothermal stability, both GSMM and GSM showed an outstanding linear relationship between nanoparticle concentration and PA value (Fig. 4e–f and Fig. S26). Predictably, GSMM exhibited excellent PAI capacity in tumor-bearing mice (Fig. 4g). Additionally, the imaging and PA intensity confirmed that GSMM has more excellent in bio-imaging than GSM (Fig. 4h and Fig. S27). The above data strongly suggested that GSMM is an excellent multimodal imaging agent for cancer diagnosis.

3.6. Immunotherapeutic efficacy of GSMM

To evaluate the immunotherapeutic efficacy of GSMM, a tumor inhibition assay was performed in a B16/F10 xenograft mouse model. 25 mice were randomly divided into five groups: G1) PBS, G2) PBS + Laser, G3) GSM + Laser, G4) GSMM, G5) GSMM + Laser. The laser treatment was executed with a 1064 nm laser irradiation (0.6 W/cm^2) for consecutive 10 min at 4 h post i.v. injection. Representative thermographic images from mice of PBS, GSM and GSMM were shown in Fig. 5a. The tumor temperature in GSMM group quickly reached above $50 \text{ }^\circ\text{C}$ compared to PBS and GSM group (Fig. 5b), which suggested that GSMM could significantly enrich in the tumor site and generate photothermal treatment effect. Then, the mice tumor volumes were monitored every three days and the curve of tumor growth was shown in Fig. 5c–d. The PBS treatment group showed a rapid increase in tumor volume. The recent report indicated that Mn^{2+} cooperated with immune checkpoint inhibitor (anti-PD-1) effectively inhibited tumor growth via potentiating STING activity and IFN-I response [21]. Indeed, GSMM alone could prevent tumor growth to some extent. But GSMM themselves are insufficient to inhibit the tumor growth. It's worth noting that tumor growth was nearly completely inhibited in GSMM + laser group.

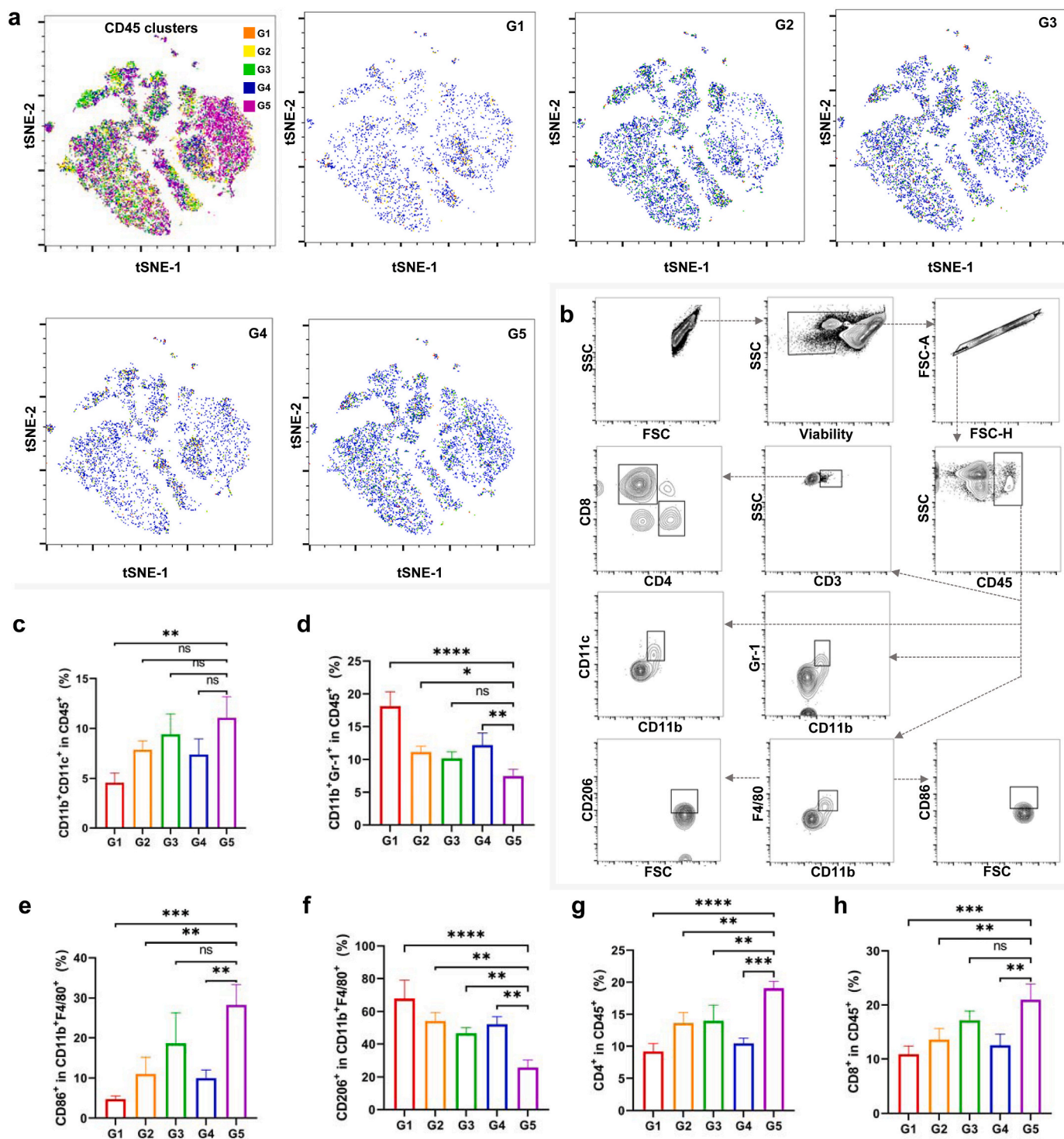


Fig. 6. The tumor immune microenvironment after different treatment. (a) CD45⁺ tumor-infiltrating leukocytes were analyzed by mass cytometry (n = 5 samples per group). The *t*-distribution stochastic neighbor embedding (*t*-SNE) plot of CD45⁺ tumor-infiltrating leukocytes of total 25 samples (pooled data) (left panel: overlaid with color-coded clusters) and density *t*-SNE plots of CD45⁺ tumor-infiltrating leukocytes in different treatment group (G1: PBS, G2: PBS + Laser, G3: GSM + Laser, G4: GSMM, G5: GSMM + Laser). (Laser irradiation was conducted at 4 h post-injection nanoparticles with a 1064 nm laser for consecutive 5 min, 0.6 W/cm²). (b) A schematic gating strategy for the identification of various immune cell populations in a B16F10 xenograft model. Flow cytometric quantification of (c) CD11b⁺CD11c⁺ dendritic cells, (d) CD11b⁺Gr-1⁺ MDSCs, (e) CD86⁺CD11b⁺F4/80⁺ M1 macrophages, (f) CD206⁺CD11b⁺F4/80⁺ M2 macrophages, (g) CD4⁺ T cells, (h) CD8⁺ T cells in tumor tissue (Ordinary one-way ANOVA with Dunnett's multiple comparisons test; ns: no significance, *: *p* < 0.05, **: *p* < 0.01, ***: *p* < 0.001, ****: *p* < 0.0001).

And the coincident results were shown in the photographs of tumors (Fig. S28) and tumor weight (Fig. S29a). Besides, during treatment, the changes of body weight in PBS treatment group were comparable to the rest groups, indicating our therapeutic strategy has a low risk of side effects (Fig. S29b). After treatment, the part of tumor tissue was made into slices for histological staining. As shown in Fig. 5e (upper), the GSMM + laser treatment group showed very weak staining of Ki67, indicating that GSMM + laser treatment successfully weakened proliferation capacity of cancer cells. PTT and CDT have been proven to cause tumor cells to develop DAMP-mediated ICD and then release of ATP, HMGB1 and CRT for promoting anti-tumor immunity [44–46]. Compared with PBS treatment group, the expression of CRT and HMGB1 in the other treatment groups had increased in varying degrees, especially in GSMM + laser group, which showed the highest expression of CRT (Fig. 5e and Fig. S30). These results suggested that GSMM combined with laser irradiation treatment can enhance ICD of tumor cells.

To confirmed the regulation of GSMM for tumor immune micro-environment, we analyzed the immune cell populations changes in tumor using flow cytometry. The part of tumor specimens from each group was digested and dissociated to obtain a single cell suspension by Gentle MACS Dissociator (Miltenyi Biotec). The *t*-distribution stochastic neighbor embedding (*t*-SNE) plot of CD45⁺ tumor infiltrating leukocyte was shown in Fig. 6a. Combined with sample ID image and quantitative analysis (Fig. S31), we can see that the composition of immune cells is basically similar in each treatment group and the number of CD45⁺ tumor infiltrating leukocyte is the highest in GSMM + laser treatment group, portending the enhancement of anti-tumor immunity. We further analyzed the changes in the number of specific cell populations in TME. The schematic gating strategy for immune cell subsets was shown in Fig. 6b. As the most primary antigen-presenting cells, Dendritic cells (DCs) play a role in T cells activation via presenting antigens to T cell receptors [47]. And the CRT, HMGB1 and ATP from ICD of cancer cells can promote the maturity of DCs to enhance immune response [44]. Here, the number of CD11b⁺CD11c⁺ DCs were significant increase in GSMM + laser (G5) group compared with each other groups (Fig. 6c). MDSCs are the major negative immune regulator which can secrete cytokines for effector T cells exhaustion [27]. After GSMM + laser treatment, the number of CD11b⁺Gr-1⁺ MDSCs were significantly decreased compared to each other groups (Fig. 6d). Clinical studies and experimental mouse models demonstrated that tumor-associated macrophages (TAMs) can not only promote tumor growth (called as M2 macrophages, stimulate angiogenesis and enhance tumor cell invasion and motility et al.), but also inhibit tumor progress (called as M1 macrophages, secrete pro-inflammatory cytokine et al.) [48,49]. In our mice model, the number of total CD11b⁺F4/80⁺ macrophages was reduced in GSMM + laser treatment group (Fig. S32). However, percentage of up-regulated M1 macrophages and down-regulated M2 macrophages indicated tumor suppressor effect (Fig. 6e and f). Recent advances have identified the role of cGAS-STING for tumor inhibition via stimulating DCs, natural killer cells and T cells et al. [50]. Mn²⁺ act as a STING inducer, we did see the high expression of STING, p-STING, p-TBK1 and p-IRF3 in GSMM + laser treatment group using western blotting (Fig. S33). Quantitative results also showed that the number of CD4⁺ T cells (Fig. 6g) and CD8⁺ T cells (Fig. 6h) was effectively up-regulated in GSMM + laser treatment group compared to each other groups. In summary, GSMM exerts dual immunotherapy based on PTT-mediated ICD and Mn-induced STING signaling pathway.

To further illustrate the broad spectrum of GSMM for tumor immunotherapy, we evaluated the tumor therapeutic effect of GSMM on mouse model breast cancer. As shown in Fig. S34a, GSMM treatment successfully restrained the tumor growth after combining with laser irradiation. We then rechallenged the mice with 4T1 cells on the contralateral flank 3 days after treatment, when the GSMM or GSM were completely cleared from the mouse body. The curve of tumor growth showed that tumors were almost completely suppressed after GSMM + laser treatment, which displays that GSMM + laser could effectively

inhibit tumor metastasis (Fig. S34b).

4. Conclusion

In this study, we successfully constructed MDSCs membrane coating manganese-based nanoparticles (GSMM) for Cancer multimodal imaging and dual-immunotherapy. The GSMM is endowed with superior performance in immune escape and active targeting TME depending on MDSCs membrane coating. Owing to the MnO₂ outer layer, the LSPR peak of GNRs is switched to NIR-II region, realizing NIR-II window PTI and PAI of GSMM. Benefiting from the release of Mn²⁺ of MnO₂, GSMM can be also used for MRI. In summary, GSMM exhibits excellent multimodal imaging abilities for cancer diagnosis, including PTI, PAI and MRI. Furthermore, GSMM can be degraded into Mn²⁺ in acidic TME. Then, on the one hand, Mn²⁺ catalyzed H₂O₂ into ·OH (a kind of ROS) for CDT leading to activate c-GAS-STING signaling, on the other hand, Mn²⁺ directly acts on STING inducing secretion of IFN I, pro-inflammatory cytokines and chemokines for strengthening anti-tumor immunity. Additionally, PTT and CDT inducing ICD of tumor cells can further enhance anti-tumor immune response via CRT, HMGB1 and ATP, which promotes the maturity of dendritic cell (DC) and antigen presentation. Therefore, GSMM realizes dual immunotherapy. Taken together, our research constructs a multifunctional nanoparticle GSMM for realizing multimodal cancer imaging and photothermal-metal-immunotherapy. At present, some treatment strategies based on Mn²⁺ have made significantly progress in clinical trials [21]. In the future, we believe that manganese-based theranostic nanoplatform will provide more extensive clinical transformation and application.

CRediT authorship contribution statement

Yuyue Zhao: Term, Conceptualization, Methodology, Software, Formal analysis, Investigation, Data curation, Writing – original draft, preparation, Funding acquisition. **Yuanwei Pan:** Term, Methodology, Software, Formal analysis, Investigation, Data curation, Writing – original draft. **Kelong Zou:** Term, Methodology, Software, Formal analysis, Investigation, Data curation. **Zhou Lan:** Term, Methodology, Software, Formal analysis, Investigation, Data curation. **Guowang Cheng:** Formal analysis, Investigation, Data curation, Resources. **Qiuying Mai:** Formal analysis, Investigation, Data curation. **Hao Cui:** Visualization, Investigation. **Qianfang Meng:** Software, Investigation. **Tongkai Chen:** Supervision. **Lang Rao:** Software, Supervision, Funding acquisition. **Limin Ma:** Writing – review & editing, Supervision, Project administration. **Guangtao Yu:** Term, Conceptualization, Writing – original draft, Writing – review & editing, Supervision, Project administration, Funding acquisition.

Declaration of competing interest

The authors declare no conflict of interest.

Acknowledgments

The authors thank financial support from National Natural Science Foundation of China (82103404), Guangdong Basic and Applied Basic Research Foundation (2020A1515110719), Southern Medical University Excellent Youth Scholars Training Program (2020YQPY008), Guangzhou Basic and Applied Basic Research Foundation (202102020687), Stomatological Hospital of Southern Medical University Startup Funds (No. PY2020001, PY2019026), High-level Hospital Construction Project (KJ012019100) and Shenzhen Bay Laboratory Startup Fund (No. 21310071).

Appendix A. Supplementary data

Supplementary data to this article can be found online at <https://doi.org/10.1016/j.bioactmat.2023.03.001>.

org/10.1016/j.bioactmat.2022.04.011.

References

- [1] P. Sharma, B.A. Siddiqui, S. Anandhan, S.S. Yadav, S.K. Subudhi, J. Gao, S. Goswami, J.P. Allison, The Next Decade of Immune Checkpoint Therapy, *Cancer Discov.* 11 (2021) 838–857.
- [2] R.G. Gupta, F. Li, J. Roszik, G. Lizée, Exploiting tumor neoantigens to target cancer evolution: current challenges and promising Therapeutic approaches, *Cancer Discov.* 11 (2021) 1024–1039.
- [3] K. Ni, T. Luo, G.T. Nash, W. Lin, Nanoscale metal-organic frameworks for cancer immunotherapy, *Acc. Chem. Res.* 53 (2020) 1739–1748.
- [4] Y. Liu, P. Bhattarai, Z. Dai, Chen X Photothermal therapy and photoacoustic imaging via nanotheranostics in fighting cancer, *Chem. Soc. Rev.* 48 (2019) 2053–2108.
- [5] G.T. Yu, M.Y. Luo, H. Li, S. Chen, B. Huang, Z.J. Sun, R. Cui, Zhang M molecular targeting nanopores with non-overlap emission in the second near-infrared window for in vivo two-color colocalization of immune cells, *ACS Nano* 13 (2019) 12830–12839.
- [6] T. He, C. Jiang, J. He, Y. Zhang, G. He, J. Wu, J. Lin, X. Zhou, P. Huang, Manganese-dioxide-coating-instructed plasmonic modulation of gold nanorods for activatable duplex-imaging-guided NIR-II photothermal-chemodynamic therapy, *Adv. Mater.* 33 (2021), e2008540.
- [7] H. Liu, G. Hong, Z. Luo, J. Chen, J. Chang, M. Gong, H. He, J. Yang, X. Yuan, L. Li, X. Mu, J. Wang, W. Mi, J. Luo, J. Xie, Zhang XD atomic-precision gold clusters for NIR-II imaging, *Adv. Mater.* 31 (2019), e1901015.
- [8] C. Song, Y. Li, T. Li, Y. Yang, Z. Huang, J.M. de la Fuente, J. Ni, D. Cui, Long-circulating drug-dye-based micelles with ultrahigh pH-sensitivity for deep tumor penetration and superior chemo-photothermal therapy, *Adv. Funct. Mater.* 30 (2020), 1906309.
- [9] B. Ding, P. Zheng, P. Ma, Lin J manganese oxide nanomaterials: synthesis, properties, and theranostic applications, *Adv. Mater.* 32 (2020), e1905823.
- [10] S.I. Han, S.W. Lee, M.G. Cho, J.M. Yoo, M.H. Oh, B. Jeong, D. Kim, O.K. Park, J. Kim, E. Namkoong, J. Jo, N. Lee, C. Lim, M. Soh, Y.E. Sung, J. Yoo, K. Park, T. Hyeon, Epitaxially strained CeO₂/Mn(3) O(4) nanocrystals as an enhanced antioxidant for radioprotection, *Adv. Mater.* 32 (2020), e2001566.
- [11] B. Xiao, X. Liu, X. Chen, G.H. Lee, M. Song, X. Yang, F. Omenya, D.M. Reed, V. Sprenkle, Y. Ren, C.J. Sun, W. Yang, K. Amine, X. Li, G. Xu, X. Li, Uncommon behavior of Li doping suppresses oxygen redox in P2-type manganese-rich sodium cathodes, *Adv. Mater.* (2021), e2107141, <https://doi.org/10.1002/adma.202107141>.
- [12] L. Galluzzi, A. Buqué, O. Kepp, L. Zitvogel, G. Kroemer, Immunogenic cell death in cancer and infectious disease, *Nat. Rev. Immunol.* 17 (2017) 97–111.
- [13] N. Albiin, N. Kartalis, A. Bergquist, B. Sadigh, T.B. Brismar, Manganese chloride tetrahydrate (CMC-001) enhanced liver MRI: evaluation of efficacy and safety in healthy volunteers, *Magma* 25 (2012) 361–368.
- [14] L. Corrales, V. Matson, B. Flood, S. Spranger, Gajewski TF Innate immune signaling and regulation in cancer immunotherapy *Cell, Res.* 27 (2017) 96–108.
- [15] K.C. Lam, R.E. Araya, A. Huang, Q. Chen, M. Di Modica, R.R. Rodrigues, A. Lopes, S.B. Johnson, B. Schwarz, E. Bohrsen, A.P. Cogdill, C.M. Bosio, J.A. Wargo, M. P. Lee, R.S. Goldszmid, Microbiota triggers STING-type I IFN-dependent monocyte reprogramming of the tumor microenvironment, *Cell* 184 (2021) 5338–5356, e5321.
- [16] A. Decout, J.D. Katz, S. Venkatraman, A. Ablasser, The cGAS-STING pathway as a therapeutic target in inflammatory diseases, *Nat. Rev. Immunol.* 21 (2021) 548–569.
- [17] L. Liang, L.L. Yang, W. Wang, C. Ji, L. Zhang, Y. Jia, Y. Chen, X. Wang, J. Tan, Z. J. Sun, Q. Yuan, W. Tan, Calcium phosphate-reinforced metal-organic frameworks regulate adenosine-mediated immunosuppression, *Adv. Mater.* (2021), e2102271, <https://doi.org/10.1002/adma.202102271>.
- [18] Q. Zhao, Z. Gong, Z. Li, J. Wang, J. Zhang, Z. Zhao, P. Zhang, S. Zheng, R.J. Miron, Q. Yuan, Y. Zhang, Target reprogramming lysosomes of CD8⁺ T cells by a mineralized metal-organic framework for cancer immunotherapy, *Adv. Mater.* 33 (2021), e2100616.
- [19] J. Liu, J. Huang, L. Zhang, Lei J Multifunctional metal-organic framework heterostructures for enhanced cancer therapy, *Chem. Soc. Rev.* 50 (2021) 1188–1218.
- [20] X. Sun, Y. Zhang, J. Li, K.S. Park, K. Han, X. Zhou, Y. Xu, J. Nam, J. Xu, X. Shi, L. Wei, Y.L. Lei, J.J. Moon, Amplifying STING activation by cyclic dinucleotide-manganese particles for local and systemic cancer metalloimmunotherapy, *Nat. Nanotechnol.* (2021), <https://doi.org/10.1038/s41565-021-00962-9>.
- [21] M. Lv, M. Chen, R. Zhang, W. Zhang, C. Wang, Y. Zhang, X. Wei, Y. Guan, J. Liu, K. Feng, M. Jing, X. Wang, Y.C. Liu, Q. Mei, W. Han, Z. Jiang, Manganese is critical for antitumor immune responses via cGAS-STING and improves the efficacy of clinical immunotherapy *Cell, Res.* 30 (2020) 966–979.
- [22] B. Xu, Y. Cui, W. Wang, S. Li, C. Lyu, S. Wang, W. Bao, H. Wang, M. Qin, Z. Liu, W. Wei, H. Liu, Immunomodulation-enhanced nanozyme-based tumor catalytic therapy, *Adv. Mater.* 32 (2020), e2003563.
- [23] G. Yang, L. Xu, Y. Chao, J. Xu, X. Sun, Y. Wu, R. Peng, Z. Liu, Hollow MnO₂ as a tumor-microenvironment-responsive biodegradable nano-platform for combination therapy favoring antitumor immune responses, *Nat. Commun.* 8 (2017) 902.
- [24] Y. Wang, Y. Xie, J. Luo, M. Guo, X. Hu, X. Chen, Z. Chen, X. Lu, L. Mao, K. Zhang, L. Wei, Y. Ma, R. Wang, J. Zhou, C. He, Y. Zhang, Y. Zhang, S. Chen, L. Shen, Y. Chen, N. Qiu, Y. Liu, Y. Cui, G. Liao, Y. Liu, Chen C Engineering a self-navigated MnARK nanovaccine for inducing potent protective immunity against novel coronavirus, *Nano Today* 38 (2021), 101139.
- [25] Q.F. Meng, Y. Zhao, C. Dong, L. Liu, Y. Pan, J. Lai, Z. Liu, G.T. Yu, X. Chen, L. Rao, Genetically programmable fusion cellular vesicles for cancer immunotherapy, *Angew Chem. Int. Ed. Engl.* (2021), <https://doi.org/10.1002/anie.202108342>.
- [26] G.-T. Yu, L. Rao, H. Wu, L.-L. Yang, L.-L. Bu, W.-W. Deng, L. Wu, X. Nan, W.-F. Zhang, X.-Z. Zhao, W. Liu, Sun Z-J myeloid-derived suppressor cell membrane-coated magnetic nanoparticles for cancer theranostics by inducing macrophage polarization and synergizing immunogenic cell death, *Adv. Funct. Mater.* 28 (2018), 1801389.
- [27] A. Grover, E. Sanseviero, E. Timosenko, D.I. Gabrilovich, Myeloid-derived suppressor cells: A Propitious Road to Clinic, *Cancer Discov.* 11 (2021) 2693–2706.
- [28] Q.F. Meng, L. Rao, M. Zan, M. Chen, G.T. Yu, X. Wei, Z. Wu, Y. Sun, S.S. Guo, X. Z. Zhao, F.B. Wang, W. Liu, Macrophage membrane-coated iron oxide nanoparticles for enhanced photothermal tumor therapy, *Nanotechnology* 29 (2018), 134004.
- [29] Q.-F. Meng, Y. Zhao, C. Dong, L. Liu, Y. Pan, J. Lai, Z. Liu, G.-T. Yu, X. Chen, L. Rao, Genetically programmable fusion cellular vesicles for cancer immunotherapy, *Angew Chem. Int. Ed. Engl.* 60 (2021) 26320–26326.
- [30] K. Zhang, X. Meng, Y. Cao, Z. Yang, H. Dong, Y. Zhang, H. Lu, Z. Shi, Zhang X metal-organic framework nanoshuttle for synergistic photodynamic and low-temperature photothermal therapy, *Adv. Funct. Mater.* 28 (2018), 1804634.
- [31] G. Gao, X. Sun, G. Liang, Nanoagent-promoted mild-temperature photothermal therapy for cancer treatment, *Adv. Funct. Mater.* 31 (2021), 2100738.
- [32] C.D. Phung, T.H. Tran, J.Y. Choi, J.H. Jeong, S.K. Ku, C.S. Yong, Kim JO pre- and post-transcriptional regulation of cFLIP for effective cancer therapy using pH-ultrasensitive nanoparticles, *ACS Appl. Mater. Interfaces* 13 (2021) 5999–6010.
- [33] M.Z. Jin, W.L. Jin, The updated landscape of tumor microenvironment and drug repurposing, *Signal Transduct. Targeted Ther.* 5 (2020) 166.
- [34] G. Yang, J. Ji, Z. Liu, Multifunctional MnO₂ nanoparticles for tumor microenvironment modulation and cancer therapy, *Wires Nanomed. Nanobiol.* 13 (2021), e1720.
- [35] L. Xin, J. Hu, Y. Xiang, C. Li, L. Fu, Q. Li, Wei X carbon-based nanocomposites as fenton-like catalysts in wastewater treatment applications: A Review, *Materials (Basel)* 14 (2021).
- [36] H. Qin, Y. He, P. Xu, D. Huang, Z. Wang, H. Wang, Z. Wang, Y. Zhao, Q. Tian, C. Wang, Spinel ferrites (MFe₂O₄): synthesis, improvement and catalytic application in environment and energy field, *Adv. Colloid Interface Sci.* 294 (2021), 102486.
- [37] R.M. Chabanon, M. Rouanne, C.J. Lord, J.-C. Soria, P. Pasero, S. Postel-Vinay, Targeting the DNA damage response in immuno-oncology: developments and opportunities, *Nat. Rev. Cancer* 21 (2021) 701–717.
- [38] D.V. Krysko, A.D. Garg, A. Kaczmarek, O. Krysko, P. Agostinis, P. Vandenabeele, Immunogenic cell death and DAMPs in cancer therapy, *Nat. Rev. Cancer* 12 (2012) 860–875.
- [39] X. Wang, J. Wang, H. Zheng, M. Xie, E.L. Hopewell, R.A. Albrecht, S. Nogusa, A. García-Sastre, S. Balachandran, Beg AA Differential requirement for the IKK β /NF- κ B signaling module in regulating TLR- versus RLR-induced type 1 IFN expression in dendritic cells, *J. Immunol.* 193 (2014) 2538–2545.
- [40] J. Wang, S.H. Basagoudanavar, X. Wang, E. Hopewell, R. Albrecht, A. García-Sastre, S. Balachandran, Beg AA NF- κ B RelA subunit is crucial for early IFN- β expression and resistance to RNA virus replication, *J. Immunol.* 185 (2010) 1720–1729.
- [41] S. Liu, X. Cai, J. Wu, Q. Cong, X. Chen, T. Li, F. Du, J. Ren, Y.T. Wu, N.V. Grishin, Z. J. Chen, Phosphorylation of innate immune adaptor proteins MAVS, STING, and TRIF induces IRF3 activation, *Science* 347 (2015), aaa2630.
- [42] H. Yang, Y. Zhuang, H. Hu, X. Du, C. Zhang, X. Shi, H. Wu, S. Yang, Silica-coated manganese oxide nanoparticles as a platform for targeted magnetic resonance and fluorescence imaging of cancer cells, *Adv. Funct. Mater.* 20 (2010) 1733–1741.
- [43] M. Lei, C. Fu, X. Cheng, B. Fu, N. Wu, Q. Zhang, A. Fu, J. Cheng, J. Gao, Z. Zhao, Activated surface charge-reversal manganese oxide nanocubes with high surface-to-volume ratio for accurate magnetic resonance tumor imaging, *Adv. Funct. Mater.* 27 (2017), 1700978.
- [44] L. Liu, H. He, Z. Luo, H. Zhou, R. Liang, H. Pan, Y. Ma, L. Cai, In situ photocatalyzed oxygen generation with photosynthetic bacteria to enable robust immunogenic photodynamic therapy in triple-negative breast cancer, *Adv. Funct. Mater.* 30 (2020), 1910176.
- [45] B. Li, G. Hao, B. Sun, Z. Gu, Z.P. Xu, Engineering a therapy-induced “immunogenic cancer cell death” amplifier to boost Systemic Tumor Elimination, *Adv. Funct. Mater.* 30 (2020), 1909745.
- [46] M. Fan, L. Jia, M. Pang, X. Yang, Y. Yang, S. Kamel Elyzayati, Y. Liao, H. Wang, Y. Zhu, Q. Wang, Injectable Adhesive hydrogel as photothermal-derived antigen reservoir for enhanced anti-tumor immunity, *Adv. Funct. Mater.* 31 (2021), 2010587.
- [47] S. Jhunjhunwala, C. Hammer, L. Delamarre, Antigen presentation in cancer: insights into tumour immunogenicity and immune evasion, *Nat. Rev. Cancer* 31 (2021) 298–312.
- [48] R. Noy, J.W. Pollard, Tumor-associated macrophages: from mechanisms to therapy, *Immunity* 41 (2014) 49–61.
- [49] L.Q. Fu, W.L. Du, M.H. Cai, J.Y. Yao, Y.Y. Zhao, Mou XZ the roles of tumor-associated macrophages in tumor angiogenesis and metastasis, *Cell. Immunol.* 353 (2020), 104119.
- [50] J. Kwon, S.F. Bakhoum, The Cytosolic DNA-Sensing cGAS-STING Pathway in Cancer, *Cancer Discov.* 10 (2020) 26–39.